Metal Oxide Chemical Looping Cycles for Coproduction of Hydrogen and Sulfuric Acid

Samuel J. Faucher[*2,3], Taylor Johnson[1], Caroline Hill[1], Dylan McCord[1], Kathryn Trimm[1], Durgesh Ranjan[1], Matthew R. Shaner[2], Ian S. McKay[2,3], and Jonathan Scheffe[*1]

[1] Department of Mechanical and Aerospace Engineering, University of Florida, Gainesville, Florida, 32611, United States
[2] Peregrine Hydrogen, Santa Cruz, CA, 95060, United States
[3] Orca Sciences, Kirkland, WA, 98033, United States
[*] To whom correspondence should be addressed

Abstract

Hydrogen production via multi-step thermochemical cycles may be an affordable, low-carbon alternative to steam methane reforming or water electrolysis. Conventional thermochemical water splitting generates hydrogen while coproducing an oxidized product, oxygen, that has little value. Instead, we use elemental sulfur as an input and coproduce sulfur dioxide. This process, which we call Steam Sulfur Reforming (SSR), could function as a value-added substitute for the sulfur burning step of sulfuric acid manufacturing. Steam Sulfur Reforming is demonstrated with experiments using ceria and iron oxide, thermodynamic modeling, and technoeconomic analysis. Sulfur oxidation is favorable at temperatures near 1200 °C, comparable to conventional sulfur burning and lower than many thermochemical water splitting cycles. Experiments with ceria demonstrate stability over dozens of cycles, with sulfur conversions of up to 90% at 1200 °C and steam conversions of up to 50% between 700 and 900 °C. Experiments with iron oxide show the intended cycle but are challenged by sulfidation side reactions and low steam conversion, highlighting opportunities for metal oxide modification. SSR may achieve costs below 2 \$/kg H_2 with CeO_2 or Fe_3O_4, making the process cost-competitive with fossil hydrogen and a potential drop-in hydrogen replacement for the fertilizer industry.

1. Introduction

Elemental sulfur is an energy-intensive byproduct of fossil fuel refining whose energetic value is underutilized in chemical transformations. Oil refineries and natural gas plants produce 80 Mt of sulfur per year by hydrodesulfurization, a process in which high-pressure hydrogen reacts with organosulfur compounds over metal sulfide catalysts to break carbon-sulfur bonds.[5-7] Hydrodesulfurization produces low-sulfur hydrocarbons and hydrogen sulfide (H_2S), which is then oxidized to elemental sulfur via the Claus process.[8-10] Industrial demand for elemental sulfur is strong because of the production of 280 Mt/yr of sulfuric acid, a key ingredient in phosphate fertilizer and a historic marker of nations' industrial capacity.[11, 12] Today, sulfur removal from oil and gas is required by law in most of the world to prevent sulfur dioxide emissions to the atmosphere that are harmful to human health. As an involuntary coproduct, sulfur is sold far below its cost of production, and an estimated 5-10 million tons of surplus sulfur accumulate each year in large surface stockpiles.[13] Even if the availability of fossil sulfur decreases in the future as the world decarbonizes[14], the way that sulfur is produced and used today represents a broad inefficiency in resource utilization: huge amounts of hydrogen and energy are consumed to recover elemental sulfur, which is then burned to produce products like sulfuric acid with low value and low embodied energy.

The reducing power of sulfur – and its highly exothermic oxidation to SO_2 – can instead be harnessed thermochemically to produce hydrogen. Global demand for hydrogen is growing rapidly, both as a chemical feedstock for ammonia and methanol production, and as a possible energy carrier or fossil fuel substitute. Most hydrogen today is made from natural gas by steam methane reforming at a cost of 1-2 \$/kg H_2. Water electrolysis is the dominant alternative, primarily using alkaline and proton exchange membrane electrolyzers. However, electrolysis faces substantial challenges: it is capital intensive, relies on scarce and costly materials like platinum group metals, and requires electrical energy that typically exceeds 50 kWh/kg H_2.[15, 16]

Thermochemical water-splitting cycles, by contrast, use high-temperature heat to dissociate water and produce hydrogen. Direct thermolysis of water is impractical, requiring temperatures above 2000°C for significant dissociation[17] and motivating the development of multi-step cycles which distribute the water-splitting enthalpy across a series of more manageable reactions. Chemical looping for hydrogen production dates back to the steam-iron process, developed in 1903 for the production of hydrogen from coal via interconversion of Fe and Fe_3O_4.[18] Two-step metal oxide redox cycles have been the primary focus of thermochemical hydrogen research since the demonstration of Fe_3O_4/FeO cycling by Nakamura et al. a half century ago.[19] In these processes, a metal oxide is thermally reduced at high temperature to release oxygen, then re-oxidized with steam at lower temperature to produce hydrogen.

Two key design choices for thermochemical cycles are the selection of a metal oxide and an energy source for metal oxide reduction. Many studies focus on stoichiometric oxides like Fe_3O_4/FeO and ZnO/Zn, which exhibit large changes in oxidation state at the cost of slow kinetics and poor cyclability. Non-stoichiometric oxides, in particular ceria ($CeO_{2-\delta}$), have become benchmark materials due to fast oxygen exchange kinetics and degradation resistance, but have higher costs and achieve modest non-stoichiometry changes of around $\Delta\delta=0.05$.[20, 21] Intended energy sources for thermochemical cycles to date include concentrated solar heat, nuclear heat, and carbon-based feedstocks like CH_4 and biomass. Using

concentrated solar heat requires advanced solar receivers that have not seen commercial success despite decades of effort, with high costs and maximum efficiencies of 5.5%, far below theoretical limits.[21] Reforming-assisted thermochemical cycles, in which the reduction of a metal oxide is coupled with the partial oxidation of biomass or fossil fuel, can enable lower process temperatures (e.g. <1250°C) and broader ceria oxidation state swings ($\Delta\delta$~0.4), but generate CO_2.[22, 23]

Ideally, a fuel for chemical looping reforming should be widely available, low cost, energetic enough to enable low-temperature metal oxide reduction, and useful rather than harmful in its oxidized form. In this work, we use elemental sulfur as such a fuel, driving a two-step redox cycle to coproduce hydrogen and sulfur dioxide in a process we term Steam Sulfur Reforming (SSR). Elemental sulfur is unable to dissociate water to generate hydrogen in a single step. However, hydrogen and sulfur dioxide can be produced through a two-step cycle as outlined below.

$$2\,\mathrm{M} + 2\,\mathrm{H_2O} \rightarrow 2\,\mathrm{MO} + 2\,\mathrm{H_2} \quad (1)$$

$$2\,\mathrm{MO} + \frac{1}{2}\mathrm{S_2} \rightarrow 2\,\mathrm{M} + \mathrm{SO_2} \quad (2)$$

In this scheme, M is an arbitrary metal or reduced metal oxide and MO is a metal oxide. This cycle is inspired by chemical looping reforming of fossil fuels[24] and hydrogen production from ammonia via thermochemical cycle.[25] It is distinct from other sulfur-containing thermochemical cycles like the hybrid sulfur cycle or sulfur iodine cycle,[26, 27] which produce hydrogen via interconversion of SO_2 and H_2SO_4 but are not net producers of sulfur products. In the first step of SSR, elemental sulfur is oxidized to SO_2 over a metal oxide (MO) such as $CeO_{2-\delta}$ or Fe_3O_4 at temperatures below 1250 °C, reducing the high-temperature step by 200-400 °C compared to conventional two-step cycles (Figure 1). The reduced oxide is then re-oxidized with steam to produce hydrogen.

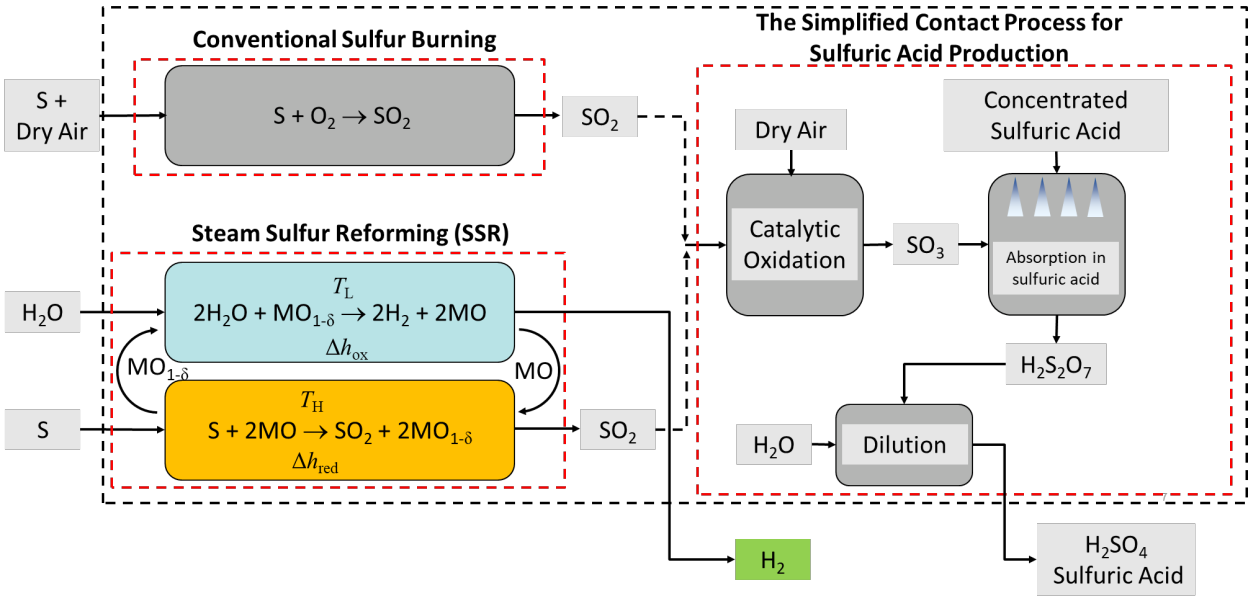

Figure 1 | Schematic comparison of steam sulfur reforming and conventional sulfuric acid manufacturing. Conventional sulfuric acid manufacturing consists of sulfur burning from S to SO_2, followed by oxidation to H_2SO_4 via the contact process. Steam sulfur reforming replaces sulfur burning, producing SO_2 with the addition of a hydrogen co-product. Both routes produce sulfuric acid en route to phosphoric acid for phosphate fertilizers like monoammonium phosphate (MAP) and diammonium phosphate (DAP).

In this study, we demonstrate Steam Sulfur Reforming through experiments, modelling, and technoeconomic analysis. Thermodynamically, SSR is likely to take place with high selectivity to desired SO_2 and H_2 products at achievable pressures and temperatures. Experiments with CeO_2 and Fe_3O_4 show repeatable redox cycling, with 90% conversion of sulfur to SO_2 and 5% conversion of steam to H_2 using CeO_2. Technoeconomic analysis suggests that SSR could achieve costs under \$2/kg H_2, competitive with steam methane reforming. This work establishes a sulfur-reforming redox cycle as a novel and industrially relevant route for production of low-carbon hydrogen for the fertilizer industry and beyond.

2. Results and discussion

2.1 Thermodynamic Modeling

Iron oxide (Fe_3O_4/FeO) enables favorable steam oxidation and sulfur-driven reduction at moderate temperatures, enabling both steps of the SSR cycle within an accessible thermal window. Conversion of steam to hydrogen decreases with increasing temperature (**Error! Reference source not found.**a) and is insensitive to steam pressure. At low oxidation temperatures (T_{ox} < 400°C), FeO readily oxidizes with steam, producing H_2 with very high conversion. However, this is not feasible under real-world conditions. Kinetic limitations make hydrogen production extraordinarily slow at temperatures below 500°C, even if favored at equilibrium.[28] Steam conversion at high temperatures above 1000 °C is unfavorable, becoming negligible above 1200°C. A cycle with Fe_3O_4/FeO, then, should operate in the 700 to 900 °C range where equilibrium steam conversion is greater than 1% but still kinetically feasible. The conversion of sulfur to

SO_2 with Fe_3O_4/FeO increases with increasing temperature and varies with sulfur pressure (**Error! Reference source not found.**a). Sulfur oxidation is more favorable at lower sulfur partial pressure by Le Chatelier's principle. High sulfur feed pressures would minimize capital costs by allowing the production of more SO_2 in a smaller reactor, implying a tradeoff between capital expense and SO_2 conversion. Across the range of calculated sulfur partial pressures ($p_{S2,in}$ =0.1, 0.01, and 0.001 bar), conversion to SO_2 is near-absolute at typical sulfur burning temperatures of 1200 to 1300 °C. Achieving a high conversion of S_2 to SO_2 is critical for the overall process: downstream condensation of unconverted sulfur would waste the sulfur input, clog pipes, and disrupt the contact process. Additional thermodynamic plots, including enthalpies and Gibbs free energies, are shown in the Supplementary Information in Figures S2 and S3. Complete oxidation to Fe_2O_3 and full reduction to Fe are not favorable with sulfur and steam as reducing and oxidizing agents, respectively.

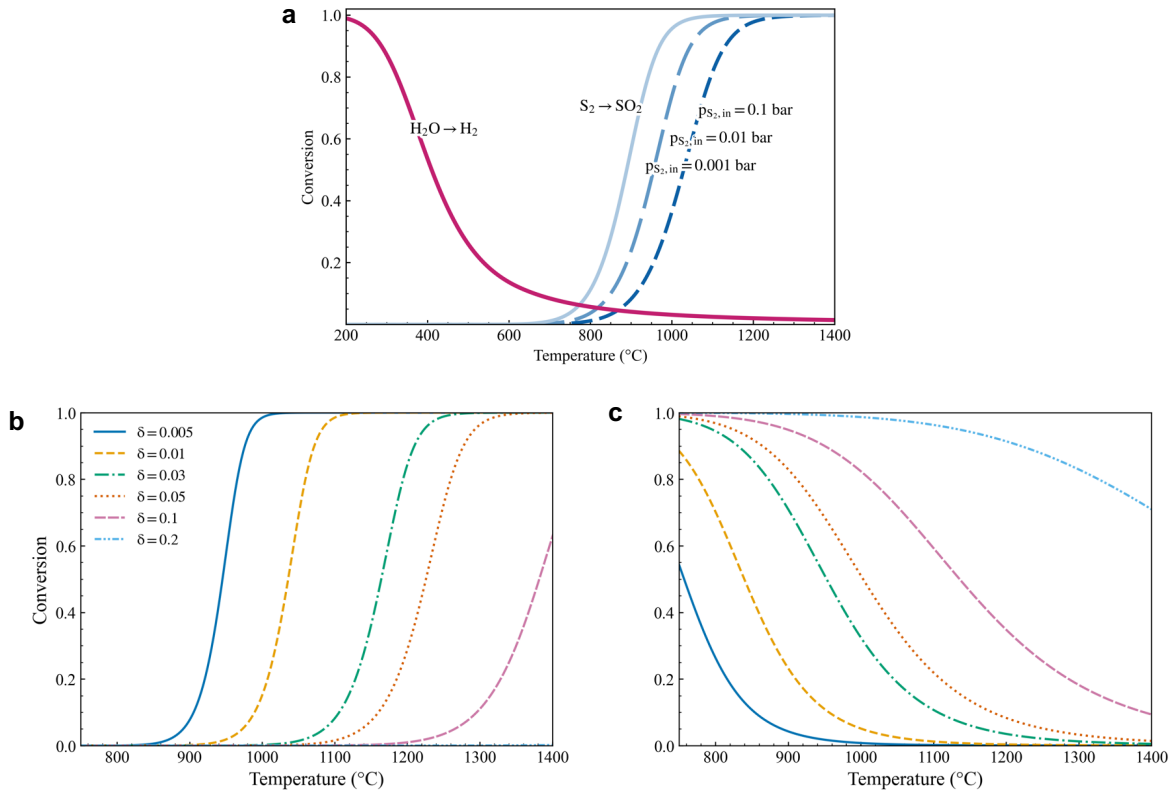

Figure 2 | Thermodynamics of steam sulfur reforming. (a) Equilibrium conversion with Fe_3O_4/FeO. Conversion of steam to hydrogen by metal oxide oxidation, and conversion of sulfur to SO_2 by metal oxide reduction, are shown as a function of temperature for several partial pressures of sulfur vapor. (b-c) Equilibrium conversion with $CeO_{2-\delta}$. (b) Conversion of sulfur to SO_2 by metal oxide reduction and (c) conversion of steam to hydrogen by metal oxide oxidation are shown as a function of temperature for several values of oxygen nonstoichiometry. Sulfur pressure is fixed at 0.1 bar.

Thermodynamic analysis with ceria, like iron, indicates favorable temperature ranges for steam oxidation and sulfur-driven reduction. Conversions of sulfur to SO_2 (Figure 2b) and steam to hydrogen (Figure 2c) vary with temperature and the nonstoichiometry parameter δ. At small oxygen deficiency (δ = 0.005),

sulfur conversion to SO_2 takes place in part at 850 °C with near complete conversion at 950 °C. As δ increases, the required temperatures for sulfur oxidation increase; at δ = 0.02, conversion remains negligible at 1150°C and near-full conversion to SO_2 is not achieved below 1300°C. This shift reflects the increasing entropy cost of reducing a ceria lattice that is already more strongly reduced (Figure S3). Since sulfur oxidation in SSR will ideally operate at sulfur burning temperatures of 1250 to 1300 °C with high sulfur conversion, this sets an upper bound for δ between 0.05 and 0.1. At high δ, appreciable conversion of steam to hydrogen may occur even at high temperatures of 1200 °C or above. Unlike with iron oxide, then, ceria could form the basis for an isothermal or near-isothermal cycle, in which sulfur oxidation and hydrogen production both take place at conventional sulfur burning temperatures.

Compared with classic two-step ceria water-splitting cycles, which require temperatures above 1400 °C and access only δ ≈ 0.02–0.05,[29] or perovskites that achieve δ ≈ 0.1–0.2 but require large temperature swings,[30] sulfur-powered cycles expand the accessible operating window and improve achievable conversions. By coupling the exothermic oxidation of sulfur to metal oxide reduction, SSR lowers the Gibbs free energy barrier for metal oxide reduction and elevates hydrogen yields at milder temperatures.

In addition to the intended redox cycle between fully oxidized and reduced metal oxides, there is a competing reaction pathway in which sulfur reacts directly with the oxide to form a metal sulfide (Figure S4). Sulfidation may irreversibly remove metal oxide from the cycle, increasing redox-inactive thermal mass, reducing H_2 yields, or producing H_2S upon exposure to steam. Sulfidation is a concern for Fe_3O_4/FeO and we observe it experimentally under certain conditions, as discussed later. By contrast, the ceria system shows negligible sulfidation; CeS and Ce_2S_3 remain at trace levels throughout the entire temperature range, with sulfur oxidized directly to SO_2 (Figure S4).

2.3 Technoeconomic Analysis

A technoeconomic analysis of steam sulfur reforming indicates costs between 1 \$/kg H_2 and 3 \$/kg H_2 depending on conditions, competitive with steam methane reforming. Costs are estimated on a \$/kg H_2 basis by comparing steam sulfur reforming to a conventional sulfur burning process. The basis of production is 4200 tonne H_2SO_4 per day, equivalent to a large single-train sulfuric acid plant. For the base case, hydrogen production is estimated at 2.17 \$/kg H_2 at a H_2:H_2SO_4 molar ratio of 0.82 with ceria, and 2.47 \$/kg H_2 at a H_2:H_2SO_4 molar ratio of 1.20 with iron oxide.

Major cost categories include materials, capital costs, operating costs, and electricity (Figure 3a and Figure 3b). While sulfur burning can be done in air or pure oxygen, air is more economical than oxygen for this process and is assumed here. In this case, the main material cost is sulfur. Capital cost (capex) estimates for a 4200 tpd H_2SO_4 plant are \$300M in total installed cost (TIC) for a conventional plant,[11] with an additional \$195M for steam sulfur reforming with ceria and \$335M for steam sulfur reforming with iron. Capex estimates for a thermochemical cycle facility are adapted from bare equipment cost (BEC) estimates from recent scientific literature[31] with a scaling exponent of 0.7. TIC is estimated from BEC as follows: an effective Lang factor of 3.8 is used to calculate inside battery plant limits (ISBL) capex from BEC, outside battery limit (OSBL) capex is estimated at 35% of ISBL, and contingency is assumed at 15% of ISBL and OSBL. Overall, this results in a total capital expenditure of 5.9 times the bare equipment cost, consistent with chemical process cost estimation standards.

Operating expenses (opex) includes labor, consumables, maintenance[11], and per-cycle metal oxide losses. Sulfuric acid is credited at $70/t on a $150/t sulfur price, in line with industry estimates for price relationships between S and H_2SO_4.[11] Steam is credited at $20/t, and electricity costs are assumed at $65/MWh. For both ceria and iron oxide, the high temperature sulfur oxidation reaction is endothermic. This heat is required above 1000 °C, and we assume that it will be provided by burning additional sulfur in oxygen in the reactor or a pre-reactor to allow direct heat transfer. In addition to the enthalpy of metal oxide reduction, there are additional heat sinks and heat sources. Heat sinks include steam, sulfur, and metal oxide heating, while heat sources include metal oxide and SO_2 cooling. We assume heat exchange between sources and sinks with characteristic values for fluid-phase heat transfer efficiency (η=0.9) and solid-phase heat transfer efficiency (η=0.5).

Any residual heat demand can be provided either by burning additional sulfur in oxygen or by electricity. In the base case, electricity is used, and hydrogen prices are $2.17/kg H_2 at a H_2:H_2SO_4 molar ratio of 0.82 with ceria, and $2.47/kg H_2 at a H_2:H_2SO_4 molar ratio of 1.20 with iron oxide. In the alternative case where all cycle energy comes from sulfur burning, the cost of hydrogen production is reduced but the hydrogen yield is reduced as well. We estimate $1.23/kg H_2 at a H_2:H_2SO_4 molar ratio of 0.55 with ceria, and $1.53/kg H_2 at a H_2:H_2SO_4 molar ratio of 0.63 with iron oxide.

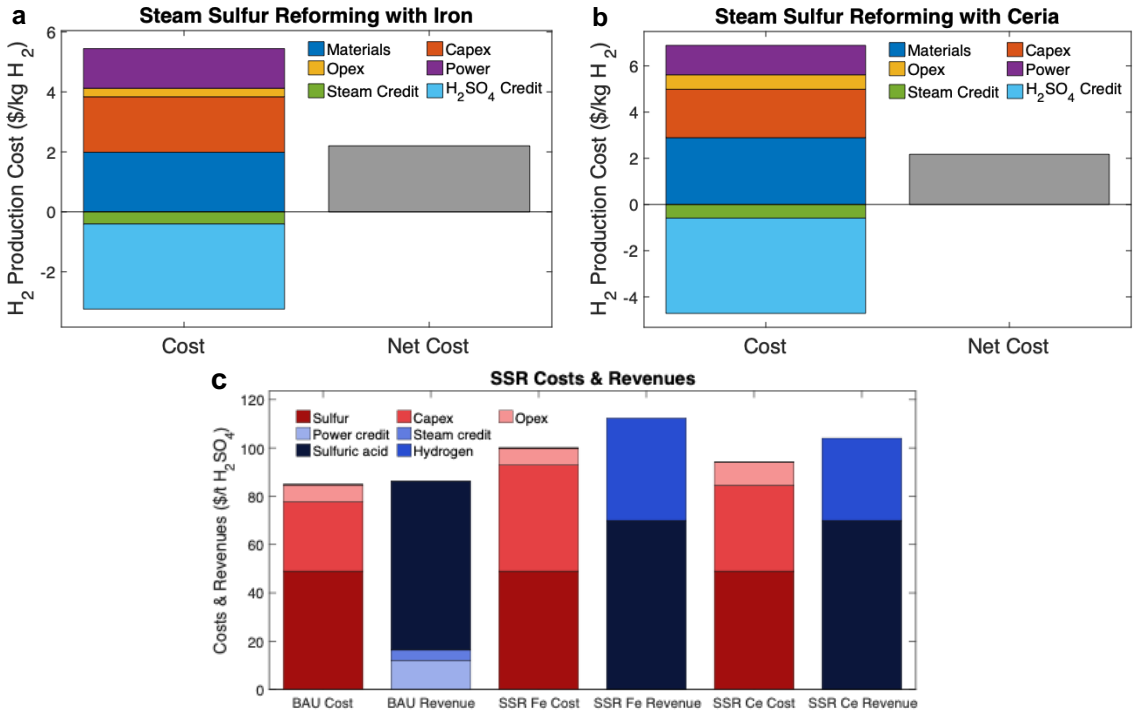

Figure 3 | Technoeconomic analysis of steam sulfur reforming. (a) Cost and net cost for SSR with iron oxide in $/kg H_2. (b) Cost and net cost for SSR with ceria in $/kg H_2. (c) Costs and revenues for steam sulfur reforming and conventional sulfuric acid manufacturing, expressed in $/t H_2SO_4.

Costs and revenues can also be expressed on a $/t H_2SO_4 basis (**Error! Reference source not found.**c). This allows comparison between the conventional contact process – in which costs are dominated by

sulfur and capital, and revenues dominated by sulfuric acid with some export of power and steam – and steam sulfur reforming, where the value of the hydrogen coproduct compensates for the additional capital cost of upgrading the sulfur burner to a steam sulfur reformer.

Sensitivity analysis indicates which factors may substantially increase or decrease the cost of hydrogen production. With iron oxide (Figure 4a), the most important parameters are capex, electricity cost, and solid heat recuperation. Solid heat recuperation is a perennial concern for thermochemical hydrogen production,[32] but efficiencies around η=0.5 may be achievable with moving or stationary bed designs. Changes in sulfur conversion, sulfur cost, and metal oxide loss per cycle are unlikely to affect hydrogen costs. Unconverted sulfur in the effluent could be condensed and recycled in analogy to sulfur recovery units in the Claus process.[33] Because of the low cost of iron oxide, metal oxide losses are expected to be unimportant, though we confine losses in this context to irreversible sintering or volatilization, not sulfidation. With ceria (Figure 4c), by contrast, the small range of oxidation states implies a large thermal mass of ceria for a given H_2 production, requiring outstanding fluid heat exchange efficiency for favorable unit economics. Other large sensitivities are capital costs and the change in ceria oxidation state. Across both metal oxides, required residence times have a moderate effect on unit economics through their connection to reactor capex, and steam and sulfur conversions have a moderate effect but could become economically important if low. Given the low conversion of steam to hydrogen, a membrane-based hydrogen separation that operates above the boiling point of water is likely required, and this is captured parametrically by the hydrogen recovery factor.

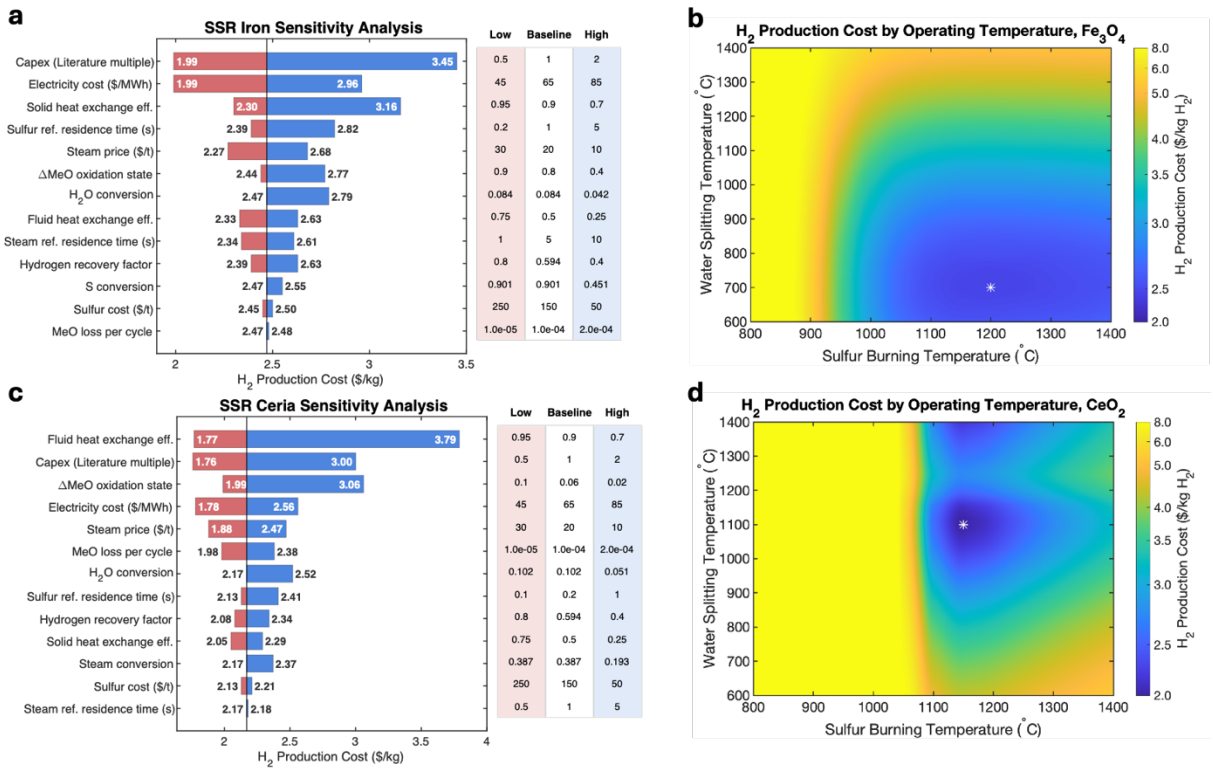

Figure 4 | Technoeconomic sensitivity of steam sulfur reforming. (a) Sensitivity analysis for SSR with iron. (b) Cost optimization of operating temperature for SSR with iron. (c) Sensitivity analysis for SSR with ceria. (d) Cost optimization of operating temperature for SSR with ceria.

The most important operating parameters for SSR are the temperatures of the sulfur burning and water splitting reactions. Estimated hydrogen production cost is shown as a function of these two temperatures for the Fe_3O_4/FeO system (Figure 4b) and $CeO_{2-\delta}$ system (Figure 4d). The base cases described above are the minima of these cost-temperature surfaces: sulfur burning at 1200 °C and hydrogen production at 700 °C with Fe_3O_4/FeO, and sulfur burning at 1150 °C and hydrogen production at 1100 °C with $CeO_{2-\delta}$. Because of the large accessible change in iron oxidation state, the thermal mass of iron oxide is low and the process is optimized with a large ΔT of 500 °C. This allows high conversion of sulfur and steam, placing relatively little stress on downstream product separations, but requires excellent fluid-phase heat exchange over the wide temperature gap. $CeO_{2-\delta}$ has a much smaller accessible change in oxidation state but much larger entropy changes upon oxidation and reduction. As a result, SSR with ceria is optimized at nearly isothermal operation, with a ΔT of 50 °C. With $CeO_{2-\delta}$, heat exchange efficiency is less important but downstream purifications – especially of hydrogen from a mixed H_2/H_2O outlet stream – are critical for the overall process.

2.4 Experimental Results

Experiments performed with granular ceria particles demonstrate SO_2 and H_2 production during successive SSR redox cycles. Reduction was performed at 1200 °C and oxidation at 700 ° C over three successive cycles (Figure 5), with volumetric flow rates for S_2 and H_2O delivery as indicated (Figure 5a).

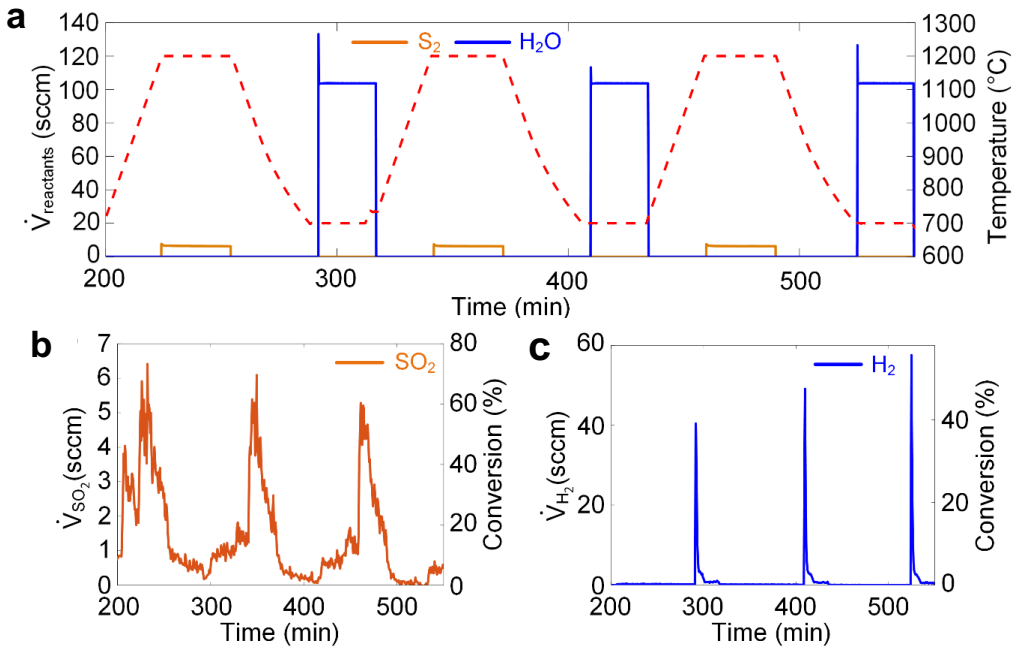

Figure 5 | Steam sulfur reforming with ceria over three cycles with reduction at 1200 °C and oxidation at 700 °C. (a) Sulfur and H_2O delivery profiles alongside temporal temperature profile. (b) SO_2 volumetric flowrates and conversion measured during ceria reduction/sulfur oxidation at 1200 °C. (c) H_2 volumetric flowrates and conversion measured during ceria oxidation/H_2O reduction at 700 °C.

As temperature increases to the reduction setpoint during the first cycle, beginning at t = 210 min, sulfur conversion to SO_2 increases (Figure 5b), peaking at 60-70% conversion and then decreasing steadily for the remainer of the sulfur delivery. Upon cooling to 700 °C and subsequent delivery of steam, H_2 is produced, peaking at about 40-60% conversion and then remaining steady at a lower conversion for the duration of the steam delivery (**Error! Reference source not found.**c). The trends are consistent across the three redox cycles, qualitatively demonstrating the stability and repeatability of the process, as confirmed by post-mortem sample characterization discussed below. Time integrated SO_2 yields for each cycle were 4.8, 4.1 and 3.9 mmol, and for H_2 were 4.6, 4.4 and 4.6 mmol. Thus, the measured H_2/SO_2 yields are less than the predicted ratio of 2. We suspect that true hydrogen production in the reactor could be greater than measured, but is consumed by reaction with condensed sulfur downstream of the reactor and before the chilled condenser, producing H_2S and reducing the measured H_2 yield in the mass spectrometer.

Experiments performed at a higher oxidation temperature of 900 °C, where faster kinetics are expected,[34] again demonstrate the Steam Sulfur Reforming process with high conversion of S to SO_2 and H_2O to H_2. These results are shown in **Error! Reference source not found.**, again showing three consecutive redox cycles under similar conditions. Here, sulfur conversions and SO_2 yields are high, peaking over 80% with time integrated SO_2 yields for each cycle of 6.8, 5.8 and 5.5 mmol. At higher temperature, oxygen availability is expected to be higher, but oxidation yields as measured by H_2 production remains almost unchanged at 4.7, 4.2 and 3.4 mmol H_2. In total, 13 redox experiments were performed with the granular ceria particles with no

observable cycle-to-cycle degradation in performance. These experimental results are summarized in Figure S5, with the variability largely depending on the starting oxidation state of the particles, time duration of the SSR experiments, and chosen oxidation temperatures.

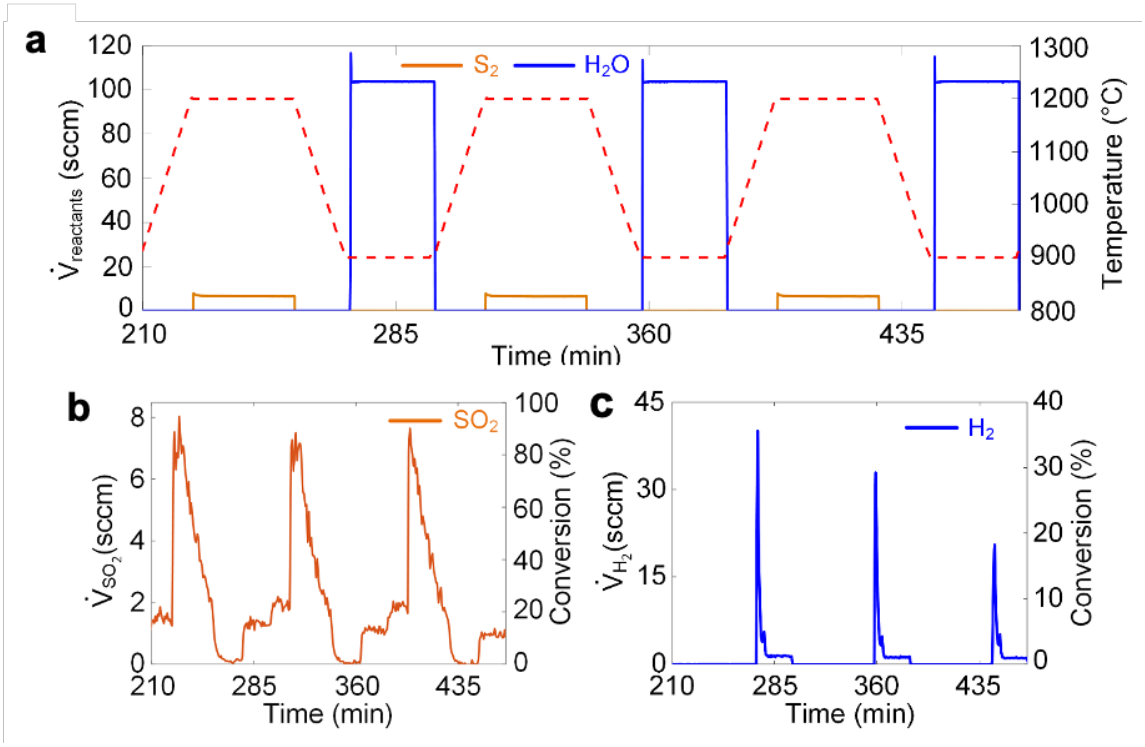

Figure 6 | Steam sulfur reforming with ceria over three cycles with 1200 °C reduction, 900 °C oxidation. (a) Sulfur and H_2O delivery profiles alongside temporal temperature profile (b) SO_2 volumetric flowrates and conversion measured during ceria reduction/sulfur oxidation at 1200 °C (c) H_2 volumetric flowrates and conversion measured during ceria oxidation/H_2O reduction at 900 °C.

Steam sulfur reforming with pelletized iron oxide demonstrates production of SO_2 and H_2 at 1200 °C and 700 °C, respectively (**Error! Reference source not found.**). Temperature is indicated by the dashed red line in the top subplot in **Error! Reference source not found.**a, and is shown alongside the corresponding S_2 and H_2O volumetric flow rates. For this experiment, steam was delivered prior to sulfur delivery (not shown) to ensure a starting composition of Fe_3O_4 rather than Fe_2O_3. SO_2 and H_2 production rates are shown in **Error! Reference source not found.**b and **Error! Reference source not found.**c, respectively. Peak SO_2 conversion is lower than ceria, approaching 30%, but as a result of the larger mass loading using pelletized Fe_3O_4, conversion remains high for the duration of the reaction and total SO_2 yields are noticeably larger. After decreasing temperature to 700 °C and introducing steam, H_2 conversion peaks at roughly 0.15% before a steady decrease. Compared to granular ceria, reaction rates are noticeable slower. Additionally, with subsequent cycling, we observed decreases in H_2 production rates (c.f. Figure S6) that are likely the result of undesirable sulfide and iron-aluminate side reactions. These side reactions are discussed below.

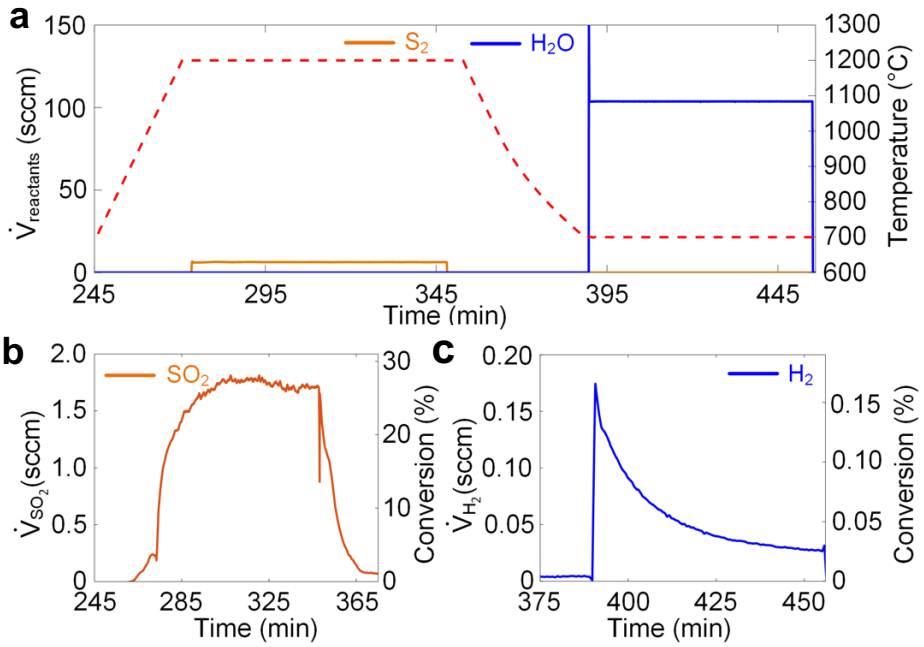

Figure 7 | Steam sulfur reforming with iron oxide with reduction at 1200 °C and oxidation at 700 °C. (a) Sulfur and H_2O delivery profiles alongside temporal temperature profile (b) SO_2 volumetric flowrates and conversion measured during iron oxide reduction/sulfur oxidation at 1200 °C (c) H_2 volumetric flowrates and conversion measured during iron oxide oxidation/H_2O reduction at 700 °C.

2.5 Analytical Characterization

Morphological and chemical changes in metal oxides after thermochemical cycling are shown by SEM, EDS mapping, and XRD. Ceria particles do not exhibit discernible structural or compositional changes (**Error! Reference source not found.**). Stability is evident in the SEM micrographs (**Error! Reference source not found.**a) and EDS maps (**Error! Reference source not found.**b), which indicate consistent morphology and elemental mapping. Quantitative EDS results (**Error! Reference source not found.**c) and XRD
patterns (Figure 8d) confirm that ceria particles are resistant to sulfidation or other chemical degradation pathways over the course of the thermochemical cycle experiments.

Iron oxide pellets, by contrast, show structural and compositional changes after sulfur cycling (**Error! Reference source not found.**). SEM imaging (**Error! Reference source not found.**a) and EDS mapping (**Error! Reference source not found.**b) of the pre- and post-cycled pellets reveal both morphological changes and shifts in elemental composition. Prior to cycling, the pellets contain only iron and oxygen, whereas after cycling they also contain sulfur and aluminum. Aluminum impurities likely come from interfacial solid phase reactions with the alumina crucible that form hercynite (Fe_2AlO_4) or other iron aluminate spinels, consistent with previous experimental observations[35, 36] but generally irrelevant to a possible industrial implementation of SSR. More concerning is the high sulfur concentration in the solid phase after cycling, which indicates production of iron sulfides by iron oxide sulfidation. The presence of iron aluminates and iron sulfides is confirmed by quantitative EDS elemental analysis (**Error! Reference**

source not found.c) and XRD (**Error! Reference source not found.**d). Sulfidation can be avoided by increasing the sulfur reaction temperature and reducing the partial pressure of sulfur (Figure S4)[37], or by changing from a pure iron oxide to an iron-based mixed metal oxide.[38]

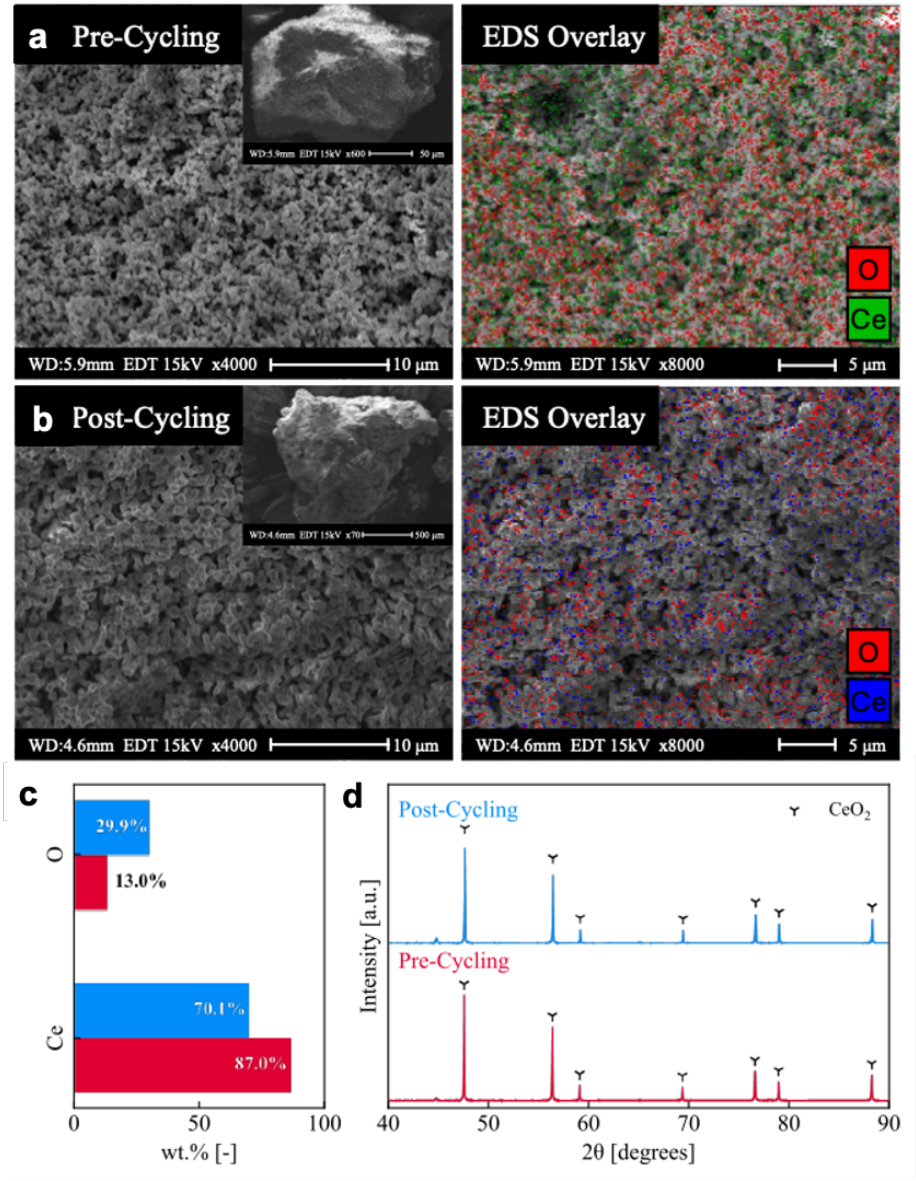

Figure 8 | Analytical characterization of ceria particles. SEM images and EDS maps of ceria particles (a) before thermochemical cycling and (b) after thermochemical cycling. Both are shown at 4000x magnification, with insets of representative particles at 600x magnification and 70x magnification, respectively. (c) Quantitative surface composition from EDS mapping. (d) Powder XRD scans before and after cycling with peaks from ref.[4]

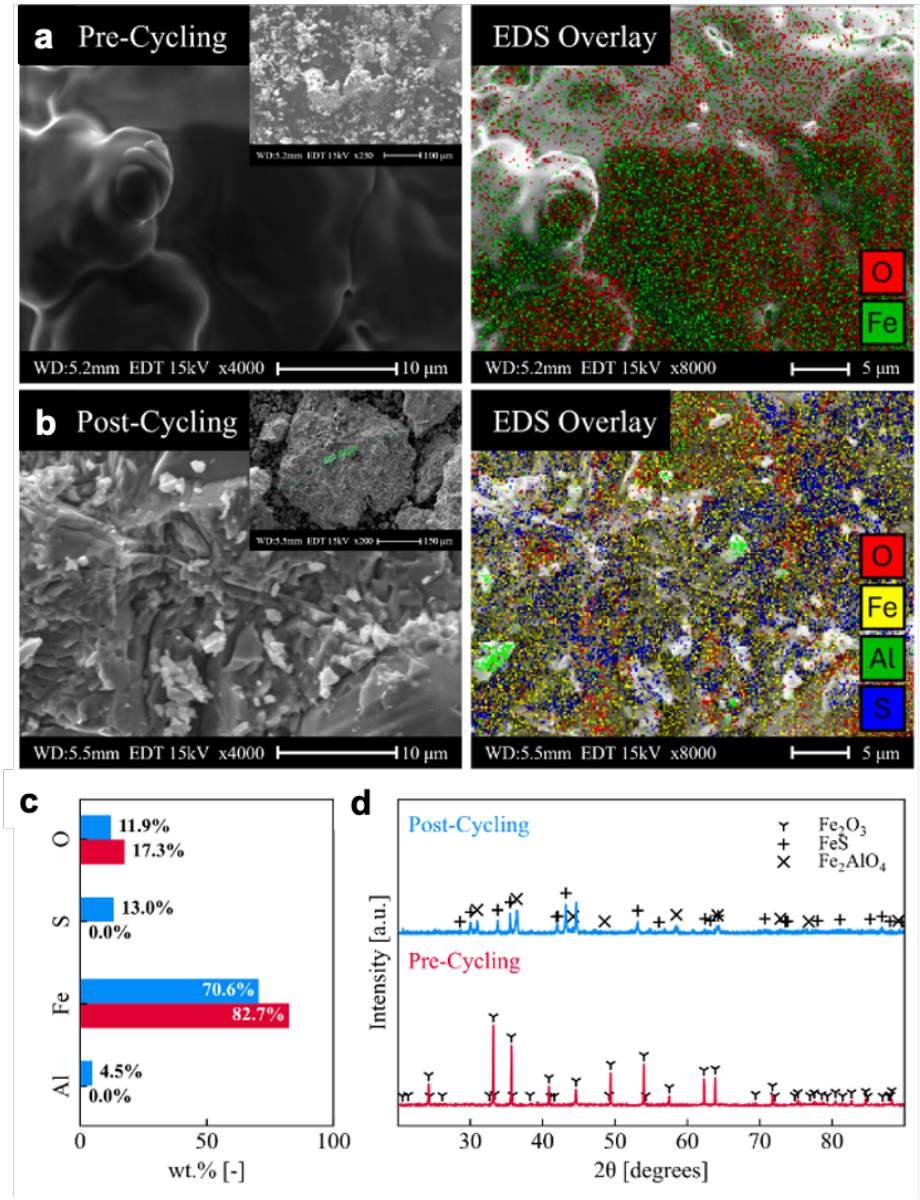

Figure 9 | Analytical characterization of the iron oxide pellet sample. (a) SEM imaging and (b) EDS mapping of pellets before cycling. (c) SEM imaging and (d) EDS mapping of pellets after cycling. An overlay at 8000x depicts the surface distribution of species, as derived from EDS mapping. The insets show a representative particle at 250x (a) or 200X (b) magnification. (e) Surface molecular composition derived from EDS mapping. (f) Powder XRD scans, peaks from ref.[1-3]

2.6 Discussion

This work demonstrates sulfur reforming cycles with ceria and iron oxides. However, numerous other metal oxides could be utilized. Volatile metal oxides such as ZnO/Zn and SnO_2/SnO pose distinct technical challenges for SSR, including vapor-phase separations with extremely high required selectivities, and were not included in this study.[39, 40] Other metal oxides, including ferrites, perovskites, and substituted ceria, may be ideal and allow SSR with even better performance and lower cost.[39-41]

Compared to other thermochemical hydrogen cycles, the temperature and reactivity demands for SSR, including desired operation at conventional sulfur burning temperatures and sulfidation avoidance, are unique and may benefit from purpose-built metal oxide chemistry.

Steam Sulfur Reforming integrates well into the sulfuric acid industry and could be extended or modified in a few ways. Many sulfuric acid plants also produce ammonia en route to fertilizers like monoammonium phosphate (MAP) or diammonium phosphate (DAP). Co-location of sulfuric acid and ammonia manufacture is ideal for SSR, since hydrogen could be used on site in the Haber-Bosch process. Additionally, chemical looping with coproduction of oxidized sulfur species could be extended beyond sulfur burning. Sulfur (+0) and sulfur dioxide (+4) are midpoints in oxidation space between hydrogen sulfide (-2) and sulfuric acid (+6), inspiring two variations of the process. First, steam reforming of hydrogen sulfide could take place by the following two-step process:

$$3\,\mathrm{M} + 3\,\mathrm{H_2O} \rightarrow 3\,\mathrm{MO} + 3\,\mathrm{H_2} \quad (3)$$

$$3\,\mathrm{MO} + \mathrm{H_2S} \rightarrow 3\,\mathrm{M} + \mathrm{H_2O} + \mathrm{SO_2} \quad (4)$$

This has a stoichiometric H_2:H_2SO_4 molar yield of 3:1, greater than 2:1 for SSR. Second, SSR could be paired with SO_2 disproportionation instead of the contact process:

$$3\,\mathrm{SO_2} + 2\,\mathrm{H_2O} \rightarrow 2\,\mathrm{H_2SO_4} + \frac{1}{2}\mathrm{S_2} \quad (5)$$

This, too, could increase H_2 yield for every tonne of sulfuric acid produced. With these process extensions, metal oxide modifications, and operating condition development, it is very possible that SSR could be optimized to become a competitive technology replacement for sulfur burning, with the added benefit of low-carbon thermochemical hydrogen production.

3. Experimental

3.1 Reactor Design

Experiments were conducted in a packed bed reactor composed of either porous Fe_3O_4 pressed pellets or sintered nonstoichiometric ceria granules ($CeO_{2-\delta}$). A P&ID diagram is shown in Figure 10 and a photograph of the experimental setup is shown in Figure S1. The samples were packed inside an alumina ceramic (ID: 0.75”) work tube held in place with porous alumina felt (Zircar Ceramics D9201). The work tube was placed in a tube furnace (Carbolite STF 16/180, 1600 °C) to provide the necessary heat to drive the redox cycling. The system also includes three mass flow controllers for gas delivery (MKS GE50A), a liquid flow controller (Bronkhorst liqui-flow L13V12) , coupled with a third gas flow controller (MKS GE50A) to dilute the vaporized H_2O exiting the steam generator (Bronkhorst W-102A-220-K). Sulfur powder was loaded into a cylindrical heated reservoir (volume: 0.5 L), heated to a desired setpoint temperature with external heat tapes and delivered to the reactor system via a manual butterfly valve during reduction. A K-type thermocouple was inserted into the bubbler system to record the sulfur delivery temperature. Pressure was monitored at the upstream and downstream of the reactor with two

pressure transducers (ATO-P400G). Reaction products were cooled in an ice bath downstream of the tube furnace to condense out excess sulfur and steam, while the gaseous composition was measured via a mass spectrometer (Hiden QGA, HAS-301-1134). The entire tubing from the sulfur tank to the inlet of the condenser was maintained at least 20 °C higher than the sulfur tank using external heat tapes. Unless otherwise stated, sulfur was delivered at 260 °C.

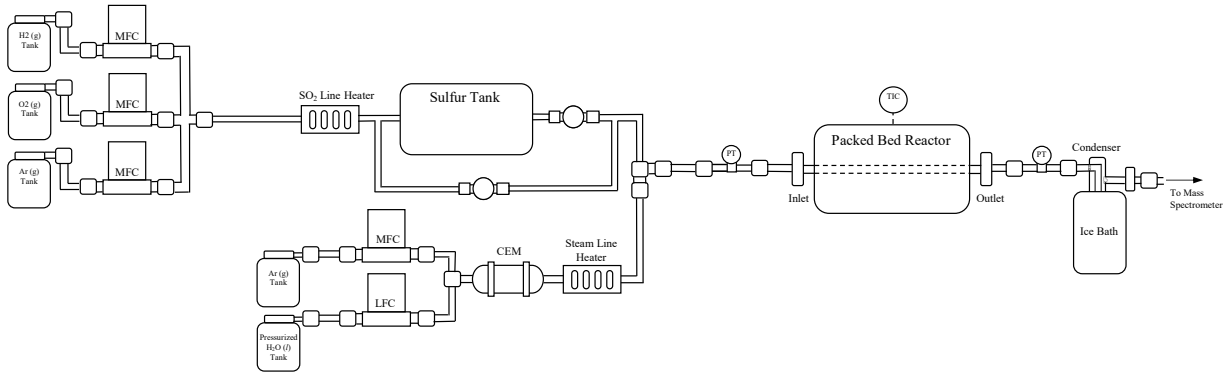

Figure 10 | Schematic of the packed bed reactor system for steam sulfur reforming. Argon and calibration gases are delivered through mass flow controllers (MFCs), while deionized water is fed from a pressurized liquid reservoir and vaporized in a heated line to supply steam. Sulfur vapor is generated in an electrically heated tank and combined with the gas and steam streams before entering the packed bed reactor. Reactor temperature is monitored and regulated by a temperature-indicating controller (TIC). The reactor effluent passes through a condenser and ice bath to remove water and sulfur species prior to compositional analysis by a mass spectrometer.

3.2 Reactor Operation

Sulfur calibration was performed prior to conducting SSR experiments. Sulfur delivery rates were estimated by quantifying SO_2 production during blank runs while delivering excess O_2 at elevated temperatures (> 600 °C) with complete conversion assumed. The tube furnace temperature was varied between 600 and 1000 °C to ensure there were no kinetic limitations.

For SSR experiments, the system was purged with Ar for one hour, followed by a three-point calibration for SO_2, H_2 and O_2 at known flowrates.[42] These calibration functions were used to quantify the product species based on mass spectrometer data. The process gas flow rates, steam flow and tube furnace temperature (ramp rate: 20 °C/minute) were controlled via LabVIEW. Typical reduction and oxidation temperatures for SSR experiments were 1200°C and 700 °C, respectively. Due to slow kinetics with iron oxide, the reduction duration (t_{red}) was set between 30 and 130 minutes, while oxidation duration (t_{ox}) was set to 45 to 60 minutes. With ceria, kinetics were faster and experiments were performed with typical parameters of t_{red} = 30 minutes and t_{ox} = 25 minutes.

3.3 Material Synthesis

Purchased iron oxide powder (Thermo Scientific, Iron (III) Oxide, 99.9% metals basis) was used to make pellets for the packed bed experiments. Iron oxide powder was mixed with graphite powder as a binder. The mixture was pressed in a pellet pressing die with 2.5 tonnes of force for 90 s in a pellet press (Carver,

Model 4350 Bench Top Laboratory Pellet Press).[43] By varying the weight composition of graphite, the pellet porosity can be tailored. The pressed samples were subsequently sintered at 1350°C for 5 hours, resulting in porous Fe_2O_3 pellets. In the current study, iron oxide pellets with 54% porosity were used. For the experiments shown, 10.77 g of Fe_2O_3 was used with a residence time of 1.45 s.

Ceria particles were synthesized from commercial cerium(IV) oxide powder (Alfa Aesar, 11328). The synthesis process has been described previously.[44] In brief, ceria powder was packed into large alumina crucibles and calcined in a box furnace (Carbolite Gero, RHF 16/8) for 10 hours at 1200 °C. This produces slabs of solid ceria which were ground with a mortar and pestle, then sieved to isolate particles larger than 1.4 mm.[44]

3.4 Material Characterization

Both the iron oxide pellets and ceria particles were analyzed before and after cycling using powder X-ray diffraction (XRD) and scanning electron microscopy (SEM) combined with energy-dispersive X-ray spectroscopy (EDS) elemental mapping. XRD analyses were performed using the Bragg-Brentano θ-2θ diffractometer setup with a Cu Kα radiation source (λ = 1.5406 Å) at 45 kV and 40 mA (Panalytical, X'Pert Powder Diffractometer). Before analysis, the iron oxide pellets and ceria particles were ground to a fine powder with a mortar and pestle and then sieved to obtain the desired particle size fraction. Scans were collected with a step size of 0.008°, a dwell time of 15.24 s per step, and a 2θ range of 20–90°. SEM-EDS analyses for surface composition were performed using an FEI Nova NanoSEM 430 with a beam voltage of 15 kV and a spot size of 4.5. Prior to imaging, ceria particles were coated with carbon to enhance surface conductivity and image quality.

3.5 Thermodynamic Modelling

Gibbs free energies, enthalpies, entropies, equilibria constants, and conversions were calculated as a function of temperature and pressure for steam sulfur reforming reactions with iron oxide and ceria. Standard-state enthalpy, entropy, and Gibbs free energy for stoichiometric (non-ceria) species were evaluated using Shomate equations with parameters from NIST Chemistry Webbook. At relevant temperatures for sulfur oxidation, the sulfur dimer predominates over the sulfur octamer[45] and is assumed to be the only sulfur allotrope. Standard enthalpy and entropy changes are computed as:

$$\Delta H_r(T) = \sum \nu_i \; H_i(T) \tag{6}$$

$$\Delta S_r(T) = \sum \nu_i \; S_i(T) \tag{7}$$

The Gibbs free energy change is as follows:

$$\Delta G_r(T) = \Delta H_r(T) - T \, \Delta S_r(T) \tag{8}$$

This is related to the equilibrium constant by:

$$K(T) = \exp\left(-\frac{\Delta G_r(T)}{RT}\right) \quad (9)$$

For the sulfur oxidation reactions and hydrogen production reactions, respectively, these equilibria constants are shown:

$$K(T) = \frac{p_{SO_2}}{p_{S_2}^{0.5}} \quad (10)$$

$$K(T) = \frac{p_{H_2}}{p_{H_2O}} \quad (11)$$

Conversions can be expressed in terms of equilibrium constants and, in the case of the sulfur reaction, the partial pressure of S_2. For ceria, standard enthalpy and entropy changes are functions of temperature and the nonstoichiometry parameter δ. The thermodynamics of ceria reduction with SO_2 production were calculated from enthalpy and entropy values for ceria reduction with O_2 production. [46] This reduction reaction is as follows:

$$\lim_{\delta_i,\delta_f\to 0} \frac{1}{\delta_\mathrm{i} - \delta_\mathrm{f}} \mathrm{CeO}_{2-\delta_i} \rightarrow \frac{1}{\delta_i - \delta_f} \mathrm{CeO}_{2-\delta_f} + \frac{1}{2}\mathrm{O}_2(\mathrm{g}) \quad (12)$$

Equilibrium constants and conversions for ceria are calculated from these thermodynamic functions using the same method as they are for iron. More details about ceria thermodynamic modeling are available in the Supplementary Information.

4. Conclusions

In this report, we propose a new industrial chemistry process, Steam Sulfur Reforming, for coproduction of hydrogen and sulfuric acid in a metal oxide mediated thermochemical cycle. Experiments with $CeO_{2-\delta}$ confirm that the process can produce SO_2 with high sulfur conversions above 90% and can produce hydrogen with moderate steam conversions above 50% at peak. Ceria cycles are well-suited for nearly isothermal conditions, with costs as low as 2.17 \$/kg H_2 for operation at 1100 °C for hydrogen production and 1150 °C for sulfur oxidation. Experiments with Fe_3O_4/FeO are challenged by kinetically limited steam conversions of 1% and sulfidation side reactions from Fe_3O_4 to FeS, but these hurdles could be overcome by introducing mixed iron-containing oxides. Costs with Fe_3O_4/FeO could be as low as 2.47 \$/kg H_2, and iron cycles are optimized with large temperature swings between hydrogen production at 700 °C and sulfur oxidation at 1200 °C.

Compared to sulfuric acid manufacturing by sulfur burning and the contact process, sulfuric acid production with steam sulfur reforming has a few advantages. Conventionally, sulfur is burned in oxygen or air to produce SO_2. A steam sulfur reformer could replace a sulfur burner with a unit process that also produces low-cost and arguably fossil-free hydrogen. Since many phosphate fertilizer plants are co-

located with nitrogen fertilizer production, hydrogen could be used directly on-site rather than stored or transported.

As a hydrogen production method, steam sulfur reforming has a few advantages. Unlike steam methane reforming or reforming-assisted thermochemical cycles, there is no hydrocarbon oxidation and no CO_2 emissions. Unlike solar-driven cycles, there is no need for unproven solar concentrators or receivers. And unlike other solar thermochemical H_2 production cycles, both the reduced H_2 product and the oxidized SO_2 product have value.

The path toward process intensification or industrial use of steam sulfur reforming starts with additional research at the laboratory scale. Future directions for research include optimizing oxide chemistry, varying residence time to probe reaction kinetics, and integrating and testing downstream separations to isolate high-quality H_2 and SO_2 product streams.

5. Author Contributions

Conceptualization: S.J.F., M.R.S., I.S.M., J.S. Investigation: C.H., T.J., D.M., K.T., D.R., J.S. Resources: J.S. Writing – Original Draft: S.J.F., J.S., T.J., K.T., D.R. Writing – Review and Editing: S.J.F., T.J., K.T., J.S. Visualization: S.J.F., T.J., D.R., J.S. Funding acquisition and supervision: M.R.S., I.S.M., J.S.

6. Conflicts of Interest

M.R.S. is an employee of Peregrine Hydrogen, a company that produces sulfur-related chemical products, and S.J.F., M.R.S., and I.S.M. have an ownership stake in the form of shares and/or options in the company.

7. Data Availability

The data supporting this article have been included as part of the Supplementary Information.

8. References

1. N. Pailhé, J. Majimel, S. Pechev, P. Gravereau, M. Gaudon and A. Demourgues, *The Journal of Physical Chemistry C*, 2008, **112**, 19217-19223.
2. M. G. Harwood, *Nature*, 1949, **164**, 787-787.
3. E. N. Maslen, V. A. Streltsov, N. R. Streltsova and N. Ishizawa, *Structural Science*, 1994, **50**, 435-441.
4. E. Y. Pikalova, V. I. Maragou, A. N. Demina, A. K. Demin and P. E. Tsiakaras, *Journal of power sources*, 2008, **181**, 199-206.
5. L. E. Apodaca, Sulfur, https://pubs.usgs.gov/periodicals/mcs2025/mcs2025-sulfur.pdf).

6. G. I. Finch and K. P. Sinha, *Proceedings of the Royal Society of London. Series A. Mathematical and Physical Sciences*, 1957, **241**, 1-8.
7. E. J. W. Verwey and E. L. Heilmann, *The Journal of Chemical Physics*, 1947, **15**, 174-180.
8. J. Lim, J. Pyun and K. Char, *Angewandte Chemie International Edition*, 2015, **54**, 3249-3258.
9. J.-G. Wagenfeld, K. Al-Ali, S. Almheiri, A. F. Slavens and N. Calvet, *Waste Management*, 2019, **95**, 78-89.
10. R. Skála, I. Císařová and M. Drábek, *American Mineralogist*, 2006, **91**, 917-921.
11. M. King, M. Moats and W. G. Davenport, *Sulfuric acid manufacture: analysis, control and optimization*, Newnes, 2013.
12. S. J. Faucher, M. R. Shaner, S. T. Omelchenko, G. Anikeeva and I. S. McKay, *ACS Sustainable Chemistry & Engineering*, 2025, **13**, 4290-4301.
13. T. A. Rappold and K. S. Lackner, *Energy*, 2010, **35**, 1368-1380.
14. M. Maslin, L. Van Heerde and S. Day, *The Geographical Journal*, 2022, **188**, 498-505.
15. M. Hubert, D. Peterson, E. Miller, J. Vickers, R. Mow and C. Howe, *DOE Hydrogen Program Record*, 2024, **24005**.
16. M. Carmo, D. L. Fritz, J. Mergel and D. Stolten, *International journal of hydrogen energy*, 2013, **38**, 4901-4934.
17. E. A. Fletcher and R. L. Moen, *Science*, 1977, **197**, 1050.
18. V. Hacker, R. Fankhauser, G. Faleschini, H. Fuchs, K. Friedrich, M. Muhr and K. Kordesch, *Journal of Power Sources*, 2000, **86**, 531-535.
19. T. Nakamura, *Solar Energy*, 1977, **19**, 467-475.
20. D. Oudejans, M. Offidani, A. Constantinou, S. Albonetti, N. Dimitratos and A. Bansode, *Energies*, 2022, **15**, 3044.
21. R. Schäppi, D. Rutz, F. Dähler, A. Muroyama, P. Haueter, J. Lilliestam, A. Patt, P. Furler and A. Steinfeld, *Nature*, 2021, 1-7.
22. S. Chuayboon, S. Abanades and S. Rodat, *Frontiers in Energy Research*, 2020, **8**, 128.
23. C. M. Hill, S. Ackermann, K. G. Trimm, D. C. McCord, P. Furler and J. R. Scheffe, *Sustainable Energy & Fuels*, 2023.
24. L.-S. Fan and F. Li, *Industrial & Engineering Chemistry Research*, 2010, **49**, 10200-10211.
25. S. K. Thengane, S. Bandyopadhyay, S. Mitra, S. Bhattacharya and A. Hoadley, *Chemical Engineering Research and Design*, 2016, **112**, 36-45.
26. J. H. Norman, K. J. Mysels, R. Sharp and D. Williamson, *International Journal of Hydrogen Energy*, 1982, **7**, 545-556.
27. L. E. Brecher, S. Spewock and C. J. Warde, *International Journal of Hydrogen Energy*, 1977, **2**, 7-15.
28. A. Singh, F. Al-Raqom, J. Klausner and J. Petrasch.
29. A. Haeussler, S. Abanades, J. Jouannaux, M. Drobek, A. Ayral and A. Julbe, *AIMS Materials Science*, 2019, **6**, 657-684.
30. M. Orfila, M. Linares, R. Molina, J. Á. Botas, R. Sanz and J. Marugán, *International Journal of Hydrogen Energy*, 2016, **41**, 19329-19338.
31. V. K. Budama, N. G. Johnson, I. Ermanoski and E. B. Stechel, *International Journal of Hydrogen Energy*, 2021, **46**, 1656-1670.
32. J. Lapp, J. H. Davidson and W. Lipiński, *Journal of Solar Energy Engineering*, 2013, **135**, 031004.

33. F. Manenti, D. Papasidero, G. Bozzano and E. Ranzi, *Computers & chemical engineering*, 2014, **66**, 244-251.
34. S. Ackermann, L. Sauvin, R. Castiglioni, J. L. M. Rupp, J. R. Scheffe and A. Steinfeld, *The Journal of Physical Chemistry C*, 2015.
35. N. Takeuchi, H. Takahashi, S. Ishida, F. Horiie and M. Wakamatsu, *Journal of the Ceramic Society of Japan*, 2000, **108**, 876-881.
36. H. Nakaishi, T. Yabutsuka, T. Yao, S. Kitao, M. Seto, W.-J. Chen, Y. Shimonishi, S. Yoshida and S. Takai, *Materials Chemistry and Physics*, 2023, **303**, 127764.
37. C. Stinn and A. Allanore, *Nature*, 2022, **602**, 78-83.
38. H. Wang, G. Liu, A. Veksha, A. Giannis, T.-T. Lim and G. Lisak, *Energy*, 2021, **218**, 119548.
39. S. Abanades, P. Charvin, F. Lemont and G. Flamant, *International Journal of Hydrogen Energy*, 2008, **33**, 6021-6030.
40. P. G. Loutzenhiser, A. Meier and A. Steinfeld, *Materials*, 2010, **3**.
41. P. Charvin, S. Abanades, G. Flamant and F. Lemort, *Energy*, 2007, **32**, 1124-1133.
42. D. C. McCord, C. M. Hill, F. Barbieri, E. J. Gager, J. C. Nino and J. R. Scheffe, *EES Solar*, 2025.
43. K. Lee and J. R. Scheffe, *Journal of Solar Energy Engineering*, 2019, **141**, 021013.
44. K. J. Warren, Carrillo, R.J., Greek, B., Hill, C.M. and Scheffe, J.R., *Energy Technology*, 2020.
45. H. Rau, T. Kutty and D. C. JG, *The Journal of Chemical Thermodynamics*, 1973, **5**, 833-844.
46. J. R. Scheffe and A. Steinfeld, *Energy & Fuels*, 2012, **26**, 1928-1936.
47. R. J. Panlener, R. N. Blumenthal and J. E. Garnier, *Journal of Physics and Chemistry of Solids*, 1975, **36**, 1213-1222.

6. Supplementary Information

6.1 Experimental Methods

An annotated photograph of the reactor (Figure S1) shows vapor feeds, a packed bed with iron pellets or ceria particles, and a downstream condenser with gas analysis.

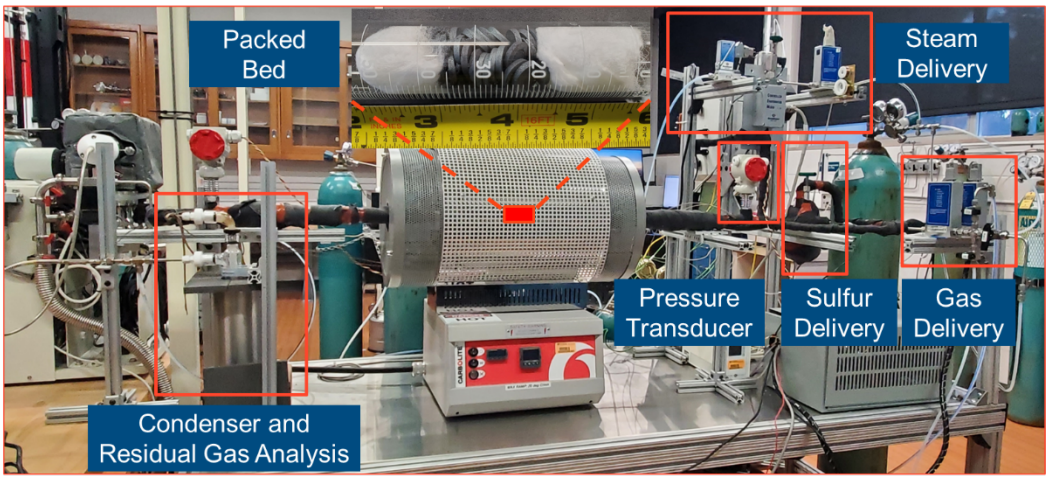

Figure S1 | Annotated photograph showing laboratory setup for SSR experiments.

6.2 Thermodynamic Modeling Methods

This section includes additional details about thermodynamic modelling of ceria. Thermodynamic modeling was performed using NIST data as described in the main text and was confirmed using NASA Thermobuild, which provides the NASA-7 polynomial coefficients required for evaluation of enthalpy and Gibbs free energy. The thermodynamic state of nonstoichiometric ceria was parameterized using experimental equilibrium data from Panlener et al.[47] Vacancy formation was represented by the infinitesimal reduction step as shown:

$$\lim_{\delta_i,\delta_f\to 0} \frac{1}{\delta_i - \delta_f} CeO_{2-\delta_i} \rightarrow \frac{1}{\delta_i - \delta_f} CeO_{2-\delta_f} + \frac{1}{2} O_2(g) \qquad (S1)$$

The corresponding partial molar Gibbs free energy of oxygen removal was evaluated as:

$$\Delta G^{\circ}(\delta, T) = -RT\ln\left[p_{O_2}(\delta, T)^{\frac{1}{2}}\right] \qquad (S2)$$

Expressed in terms of enthalpic and entropic contributions, this is:

$$\Delta G^{\circ}(\delta, T) = \Delta h^{\circ}(\delta) - T\Delta s^{\circ}(\delta) \qquad (S3)$$

By combining these relations, the equilibrium oxygen partial pressure was evaluated as:

$$\ln\left[p_{O_2}(\delta,T)^{\frac{1}{2}}\right] = -\frac{\Delta\bar{h}_o(\delta)}{R}\frac{1}{T}+\frac{\Delta\bar{s}_o(\delta)}{R} \qquad (S4)$$

Experimental isotherms of $\ln\left[p_{O_2}(\delta,T)^{1/2}\right]$ vs. T^{-1} at fixed δ were regressed to evaluate $\Delta\bar{h}_o(\delta)$ and $\Delta\bar{s}_o(\delta)$, enabling calculation of the dependence of equilibrium oxygen pressure on both nonstoichiometry and temperature in the ceria reduction calculations.

Equilibrium calculations were performed using Cantera, an open-source chemical kinetics and thermodynamics software package. At a set temperature and pressure, the equilibrium composition is obtained by solving a nonlinear optimization problem. The objective function is the total Gibbs free energy of the system, where n_i are the species mole numbers and μ_i are their chemical potentials.

$$G(T,P,n) = \sum_i n_i\mu_i(T,P) \qquad (S5)$$

The standard-state chemical potential of a species is evaluated using its reference enthalpy $h_i^\circ(T)$ and entropy $s_i^\circ(T)$:

$$\mu_i^\circ(T) = h_i^\circ(T) - Ts_i^\circ(T) \qquad (S6)$$

The actual chemical potential at system conditions is then given by:

$$\mu_i(T,P,y) = \mu_i^\circ(T) + RT\ln a_i, \qquad a_i = \frac{p_i}{p^\circ} \qquad (S7)$$

Here, the species activity, a_i, is taken as the ratio of the species partial pressure to standard pressure. To quantify reaction progress, equilibrium mole balances were used to define conversion extents for both sulfur oxidation (10) and water splitting (11). Conversion was calculated from the difference between the initial reaction feed and the equilibrium amount of product formed, normalized to the inlet reaction feed.

$$\alpha_{S_2\rightarrow SO_2} = \frac{n_{SO_{2,eq}} - n_{SO_{2,i}}}{2n_{S_{2,i}}} \qquad (S8)$$

$$\alpha_{H_2O\rightarrow H_2} = \frac{n_{H_{2,eq}} - n_{H_{2,i}}}{n_{H_2O_i}} \qquad (S9)$$

6.3 Thermodynamic Modeling

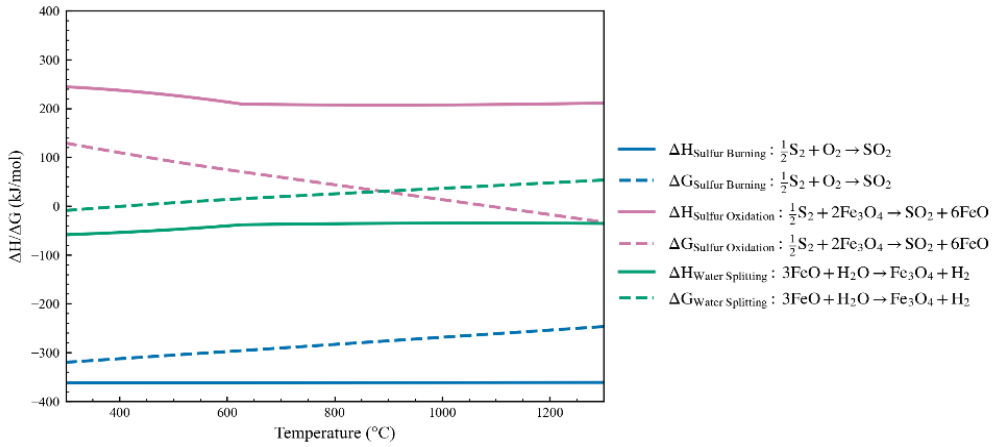

Figure S2 | Thermodynamics of steam sulfur reforming with iron oxide. Calculated reaction enthalpies (ΔH) and Gibbs free energies (ΔG) in the Fe_3O_4/FeO system.

Enthalpies and Gibbs free energies are shown for steam sulfur reforming reactions as a function of temperature (Figures S2 and S3). Sulfur combustion remains highly exothermic and spontaneous across all conditions. The sulfur-driven reduction of Fe_3O_4 is moderately endothermic, with ΔG becoming negative above ~900°C, corresponding to the onset of SO_2 formation in Figure S2. Steam oxidation of FeO is mildly endothermic, with ΔG becoming positive above ~600°C, reflecting the collapse of H_2 yields at elevated T_{ox}. Sulfur exhibits the opposite temperature dependence as compared to steam splitting; at low reduction temperatures (T_{red} < 800°C), as shown in Figure S3, ΔG for the Fe_3O_4 reduction by sulfur is strongly positive and the equilibrium conversion of S_2 to SO_2 remains negligible, as the endothermic cost of reducing Fe^{3+} to Fe^{2+} and breaking Fe-O bonds outweighs the exothermic stabilization gained by the S-O bond formation.

As T_{red} increases, the entropy gain associated with SO_2 formation increasingly offsets the lattice formation enthalpy, causing ΔG to steadily decrease, becoming negative and marking the onset of spontaneous sulfur oxidation between 700-800°C. The precise temperature at which this occurs is sensitive to the inlet sulfur chemical potential; higher $p_{S_2,in}$ raises the chemical potential of the reactant, delaying the transition to higher T_{red}, whereas lower $p_{S_2,in}$ lowers the barrier and shifts the onset earlier. Figure 3 illustrates this trend, with the Gibbs free energy for the magnetite sulfur oxidation step decreasing from strongly positive to negative across this temperature range, while the reaction enthalpy remains moderately endothermic.

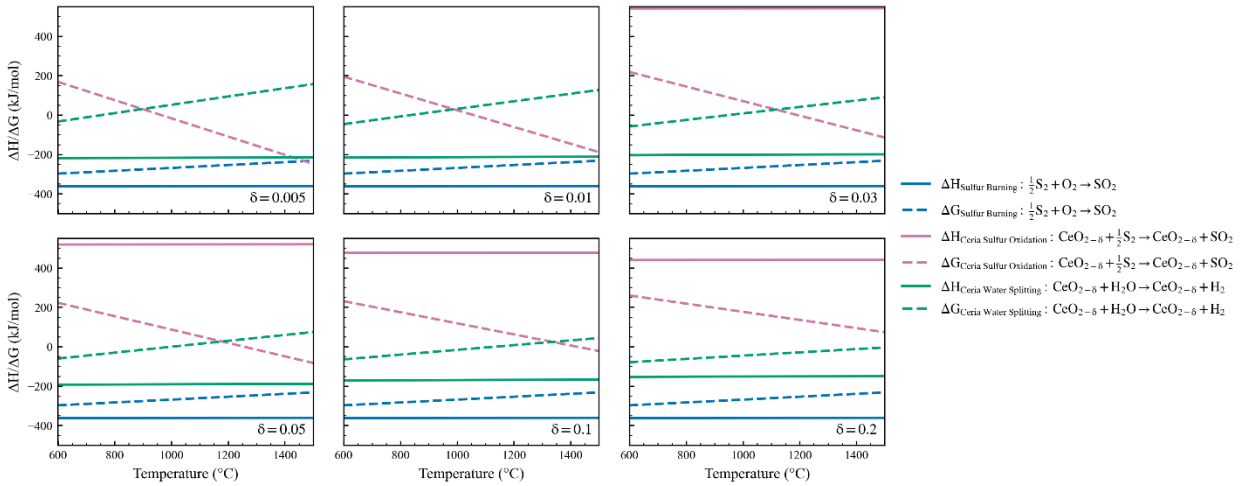

Figure S3 | Thermodynamics of steam sulfur reforming with ceria. Calculated reaction enthalpies (ΔH) and Gibbs free energies (ΔG) in the $CeO_{2-\delta}$ system as a function of nonstoichiometry parameter δ.

6.4 Selectivity to Oxides and Sulfides

Sulfidation reactions – in which sulfur reacts with metal oxides to produce metal sulfides rather than SO_2 – are a concern for steam sulfur reforming. Equilibria for metal oxide reduction versus metal oxide sulfidation are shown (Figure S4).

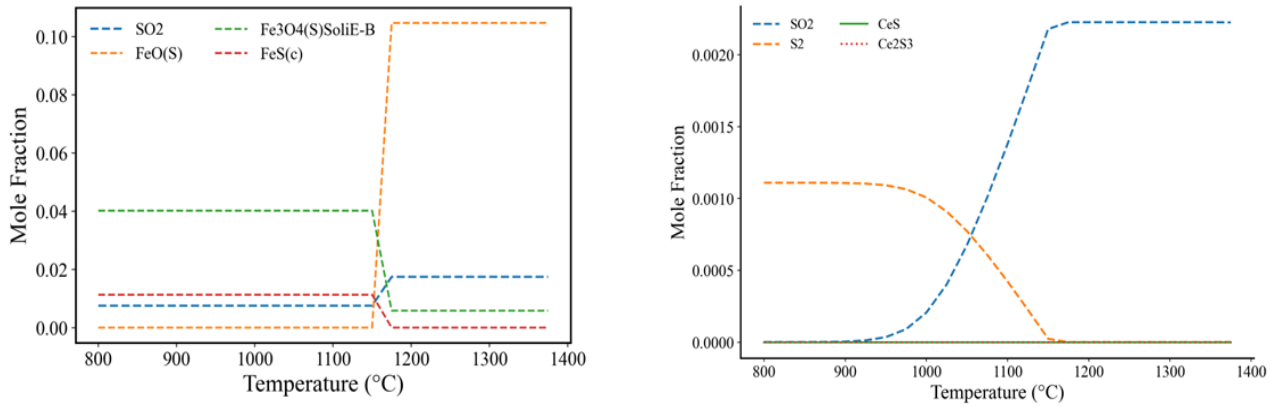

Figure S4 | Selectivity to oxides vs sulfides, shown on left for iron and on right for ceria. Selective oxidation without sulfidation is essential for steam sulfur reforming.

6.5 Durability Testing with Ceria

A total of 13 SSR cycles were performed with the ceria particles, a summary of which is shown (Figure S5). Throughout experimentation, SO_2 and H_2 production were consistently observed, with some variability depending on the starting oxidation state of the particles, time duration of the SSR experiments, and oxidation temperatures that were chosen. Initially, for the first two SSR cycles (1200 °C

and 700 °C oxidation), relatively long reduction and oxidation times were used because the reaction kinetics were not well understood. The higher SO_2 conversion during the first cycle is explained by the fact that ceria particles were completely oxidized prior to experimentation. Then during the subsequent oxidation with steam, the particles did not return to their original oxidation state, resulting in less SO_2 during the subsequent reduction. During the next set of 5 consecutive cycles, reduction and oxidation times were reduced to eliminate the excessive SO_2 and H_2 tails where conversion was low, and the same general trends were observed. The next three cycles were intended to be completed like the prior 5, but experimentation was aborted prematurely during the 4th cycle due to sulfur deposition and over-pressurization of the packed bed. The final three cycles were performed at a higher oxidation temperature of 900 °C, while keeping the reduction temperature at 1200 °C, in order to improve oxidation conversions and extents. In total, for the last six cycles, peak H_2 rates increase and the rates level off at a higher baseline compared to prior experiments performed at 700 °C. The reason for this apparent increase in H_2 production rates is not clear. But it could be a result of a variety of factors, including decreased H_2S production, morphological changes or more favorable oxidation states as a result of further reduction with subsequent reduction reactions.

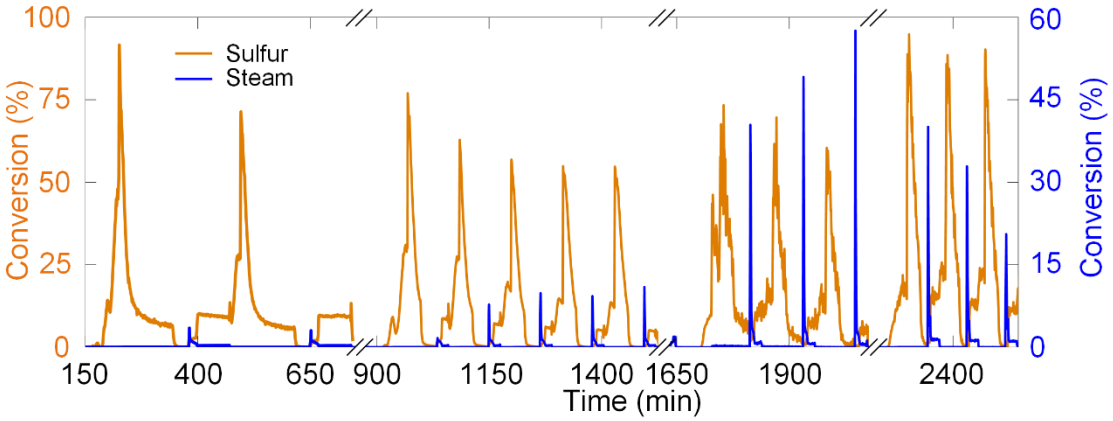

Figure S5 | Sulfur oxidation and hydrogen production by steam sulfur reforming with ceria over multiple cycles. Cycles 1-9 performed at 1200 °C reduction, 700 °C oxidation and cycles 10-12 1200 °C reduction, 900 °C oxidation. Sulfur and steam delivery flowrates are consistent with those described in experimental methods.

6.5 Durability Testing with Iron

Iron oxide oxidation cycles show decreasing H_2 production rates from cycle to cycle. This is likely a result of iron oxide sulfidation, as described in the main text, though it may also be a result of sintering. All hydrogen-producing reactions were conducted at 700 °C.

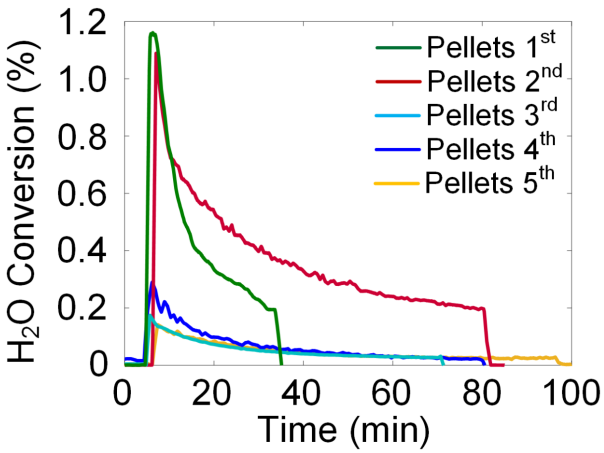

Figure S6 | Hydrogen production rates by cycle number with iron oxide. All experiments are performed at 700 °C.